

Experimental studies of nonlinear beam dynamics

D.D. Caussyn, M. Ball, B. Brabson, J. Collins, S.A. Curtis, V. Derenchuk,
D. DuPlantis, G. East, M. Ellison,
T. Ellison, D. Friesel, B. Hamilton, W.P. Jones, W. Lambie, S.Y. Lee, D. Li,
M.G. Minty,* T. Sloan, and G. Xu

Indiana University Cyclotron Facility, Indiana University, Bloomington, Indiana 47405

A.W. Chao

Superconducting Super Collider Laboratory, 2550 Beckleymeade Avenue, Dallas, Texas 75237-3946

K.Y. Ng

Fermilab, P.O. Box 500, Batavia, Illinois 60510

S. Tepikian

Brookhaven National Laboratory, Upton, New York 11973

(Received 11 June 1992)

The nonlinear beam dynamics of transverse betatron oscillations were studied experimentally at the Indiana University Cyclotron Facility cooler ring. Motion in one dimension was measured for betatron tunes near the third, fourth, fifth, and seventh integer resonances. This motion is described by coupling between the transverse modes of motion and nonlinear field errors. The Hamiltonian for nonlinear particle motion near the third- and fourth-integer-resonance conditions has been deduced.

PACS number(s): 41.75.-i, 03.20.+i, 05.45.+b, 29.20.Dh

I. INTRODUCTION

The significance of nonlinear dynamics to accelerator design and operation is widely recognized. Nonlinearities can have the undesirable effect of reducing the accelerator acceptance, or dynamic aperture, from what would be expected for a purely linear machine. On the other hand, nonlinear effects have been found useful in applications such as slow extraction of beam from a high-energy accelerator, or for beam manipulations in phase space [1]. Nonlinear-beam-dynamics studies have become increasingly important to the design of future colliders such as the superconducting super collider (SSC) and the relativistic heavy ion collider (RHIC). This is in large part due to the superconducting magnets used in these accelerators. These magnets have fields with higher-order multipole components which are considerably stronger than those in conventional iron magnets, producing correspondingly stronger nonlinear terms in the Hamiltonian. While the nonlinear terms in the Hamiltonian are intrinsically weak, particle motion can be strongly affected when resonance conditions are encountered.

Many theoretical studies [2] of motion in nonlinear fields have predicted both the long- and the short-term behavior of orbiting particles in an accelerator. In order to better understand the validity and limitations of the approximations used in these theoretical predictions, experimental studies of resonant behavior are essential. Several nonlinear-beam-dynamics experiments have been performed in the past [3]. These experiments studied the general features of nonlinear motion, such as resonance

island stability, smear, tune dependence on amplitude, etc. However, motion around stable fixed points in phase space, or resonance islands, has not yet been studied in detail, to the authors' knowledge. Since individual particle motion cannot be tracked experimentally, these studies typically track the motion of the beam centroid after collectively perturbing the beam.

The degree to which the collective motion of the beam accurately represents the motion of a single particle is a function of the emittance of the beam; the smaller the emittance of the beam, the more accurate its representation of single-particle motion. In this respect, the Indiana University Cyclotron Facility (IUCF) cooler ring provides an ideal environment for nonlinear-beam-dynamics experiments. The 95% emittance, or phase-space area, of the proton beam is electron cooled to about 0.3π mm mrad in less than 3 s. The resulting relative momentum spread full width at half maximum (FWHM) of the beam is about ± 0.0001 and the beam lifetime could be as long as hours. Such a high-quality beam bunch can closely simulate single-particle motion.

This article provides details of the nonlinear-beam-dynamics experiments recently performed at the IUCF cooler ring, some of which have been reported previously [4]. Particle motion near four different resonances was studied. The experimental methods used in this study are described in Sec. II. The data and the analysis are discussed in Sec. III, where we present a method for obtaining properties of resonance islands, and determine the Hamiltonian for the particle motion near two of the resonance conditions. Section IV contains a summary and conclusions.

II. EXPERIMENTAL METHODS

The IUCF cooler ring is hexagonal with a circumference of 86.82 m. The experiment was done with a 45-MeV proton beam injected and then stored in a 10-s cycle. The stored beam consisted of a single bunch, typically with 3×10^8 protons and a bunch length of about 3.6 m (or 40 ns) FWHM. The revolution period in the accelerator was 969 ns with bunching produced by operating an rf cavity with frequency 1.031 68 MHz with a harmonic number h of 1.

Before making a measurement, the injected beam was electron cooled for at least 3 s. The stability of the horizontal closed orbit was estimated to be better than 0.05 mm FWHM. The beam was then kicked with various angular deflections θ_K , with a pulsed deflecting magnet having a time width of 600 ns FWHM, and rise and fall times of 100 ns. The kick occurred in conjunction with a triple coincidence between a signal from the data acquisition system, the rf system, which was providing the beam bunching, and a 7-s delay from the beginning of the injection cycle. A schematic of the principle components of the electronics is shown in Fig. 1.

Once perturbed by the kicker, the beam executed coherent betatron motion [5], which will be discussed further in the next section. The motion being studied was along the x axis in the curvilinear coordinate system in which the s axis points in the instantaneous direction of beam motion, the x axis points radially outward, and the z axis points vertically upward. The horizontal position at two different positions along the s axis is used to locate the beam in the phase space x - p_x , a process which will

be described further in the next section. Electron cooling has a very small effect in the time a measurement is made (4096 turns); nevertheless, it was turned off 20 ms before the beam was kicked to avoid any damping of the betatron oscillations it might do.

The motion of the beam centroid was tracked using two beam-position monitors (BPM's). Since motion in one dimension only was being studied, each BPM measured the displacement of the beam from the stable closed orbit in the horizontal plane. The BPM's were diagonally split cylindrical capacitive pickups, each half on opposite sides of the beam in the horizontal plane [6]. As the beam passes through a BPM, signals on the right-hand and left-hand electrodes, R and L , are induced which are approximately proportional to the product of the charge of the beam bunch enclosed within the BPM and its horizontal distance from the electrode. The sum signal Σ is the analog sum of the signals from the two halves of the BPM and is proportional to the beam bunch charge. The schematic of the electronics in Fig. 1 shows the signals from the BPM's and the processing that was done.

Because the signals from the BPM's were only about 40 ns in duration, digitization without further processing was deemed impractical. Instead, a peak-detecting circuit was used in conjunction with a sample-and-hold circuit to produce an analog signal with a level proportional to the peak value of the amplified R and Σ signals. Since the beam intensity at the start of a measurement could vary by over an order of magnitude during an experiment conducted near a nonlinear resonance, the amplified signals could require attenuation before the peak detection circuit. This was accomplished by using programmable

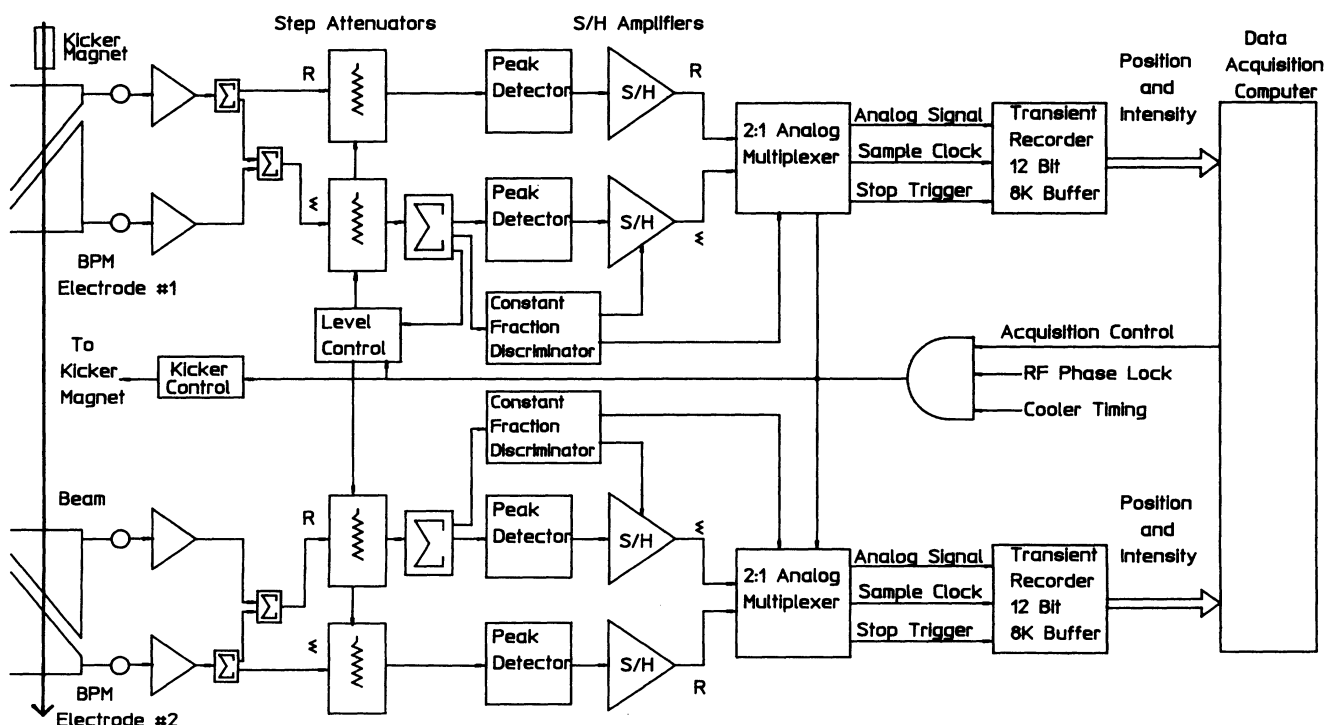


FIG. 1. A block diagram of the BPM electronics.

variable attenuators controlled by a level detecting circuit. Further details on the analog electronics can be found in Ref. [7].

After analog processing, the R and Σ signals from a BPM were digitized with a 12-bit transient recorder having 8192 words of memory. The transient recorders were strobed externally using signals derived from the respective Σ signals by using constant fraction discriminators. With the two available transient recorders, each transient recorder had to digitize both the R and Σ signals from a BPM. The R and Σ signals were multiplexed, and each transient recorder, having 8192 words of memory, digitized R and Σ for 4096 turns around the accelerator with 512 of these turns occurring before the beam was kicked. This information was read by the data acquisition computer, which stored the data on magnetic tape for more detailed analysis at a later time.

On-line calculations of the normalized position, i.e., $\frac{2R-\Sigma}{\Sigma}$, and the fast-Fourier transform (FFT) of the normalized position were done to monitor the progress of the experiment. The FFT of the normalized position provides the frequency of the betatron oscillations as a fraction of the revolution frequency, which is called the horizontal betatron tune ν_x . The integer part of the tune, and the ambiguity in the fractional part of the measurement, is resolved from an observation of the periodicity of a closed orbit distortion [8]. Also, since the position measurement is not perfectly linear, harmonics may appear in the FFT spectrum. Thus sidebands of the betatron frequency may appear when the signal is the superposition of components with different frequencies, as may happen if there is a significant amount of coupling between the transverse modes of motion.

The absolute position of the beam was determined by calibrating a BPM identical to those used in the experiment and with amplifiers that were carefully matched to have the same gain as those used for the experiment, against a nearby wire scanner. We estimate the error in the calibration using this method to be about 5%. The position resolution was measured to be 0.23 mm FWHM, or less, for each BPM in the range of operating currents used in this experiment. This figure for the position resolution was determined from the measurement of the closed orbit position and is within a factor of 2 of the lower limit for the resolution estimated from the electronic noise at the input of the first amplifier alone.

III. DATA AND ANALYSIS

A. Betatron motion in phase space

For particle motion in a circular accelerator, the horizontal deviation from the closed orbit, $x(s)$, satisfies Hill's equation:

$$\frac{d^2x}{ds^2} + K(s)x = \frac{\Delta B_z}{B\rho}. \quad (3.1)$$

Here $K(s)$ is a function of the quadrupole strength, $B\rho = p/e$ is the magnetic rigidity, and s is the longitudinal particle coordinate, which advances from 0 to C , the

circumference, as the particle completes one revolution of the cyclic accelerator. The anharmonic term $\frac{\Delta B_z}{B\rho}$, which arises from higher-order multipoles, coupling terms, or quadrupole and dipole errors, is normally small. Oscillations about the closed orbit due to the linear focusing force of quadrupoles, $K(s)$, are called betatron oscillations. The number of oscillation periods in one revolution is the horizontal betatron tune ν_x , which can be adjusted by varying the quadrupole strength within the accelerator. Both $K(s)$ and the anharmonic term $\frac{\Delta B_z}{B\rho}$ are periodic functions of s with period C .

Neglecting the small anharmonic term in the Hamiltonian, the betatron motion is linear. Hill's equation, Eq. (3.1), can be solved using the Floquet transformation [5] to obtain the solution

$$x = \sqrt{2\beta_x J} \cos \phi, \quad (3.2)$$

where J and ϕ are action-angle variables. Here $2J$ is the phase-space area (called the Courant-Snyder invariant or the emittance) of the betatron motion and β_x is the betatron amplitude function of the Floquet transformation (β_x is periodic in s with period C). For each turn around the accelerator, the angular variable ϕ increases by $2\pi\nu_x$. The turn-by-turn tracking of motion in x - x' phase space, as observed at a given location in the cyclic accelerator, is called a Poincaré map. Linear betatron oscillations produce ellipses in the Poincaré map. Thus deviations from ellipses in a Poincaré map can be used to study the anharmonic term of the Hamiltonian.

B. Deduction of Courant-Snyder parameters

Experimentally, x' is not a convenient quantity to measure. From the linear solution for betatron motion, given by Eq. (3.2) above, x' is given by

$$x' = \frac{1}{\beta_x} \{-\alpha_x x - \sqrt{2\beta_x J} \sin \phi\}, \quad (3.3)$$

where $\alpha_x = -\frac{1}{2} \frac{d\beta_x}{ds}$. By defining normalized momentum, p_x , as

$$p_x = \alpha_x x + \beta_x x', \quad (3.4)$$

then from Eq. (3.3),

$$p_x = -\sqrt{2\beta_x J} \sin \phi. \quad (3.5)$$

By comparing Eqs. (3.5) and (3.2) it is seen that when linear motion is plotted in x - p_x space, it is a circle [5] defined by the equation,

$$p_x^2 + x^2 = 2\beta_x J. \quad (3.6)$$

Note that the action-angle variables are J and ϕ , where ϕ is the clockwise angle measured in x - p_x space from the x axis.

The variables that are actually measured are x_1 and x_2 at the two BPM's which are separated in betatron phase by ϕ_{12} . The $\alpha_x x$ term in Eq. (3.4) can be solved in terms of x_1 and x_2 from the linear transformation of the phase-space coordinates from BPM1 to BPM2. By

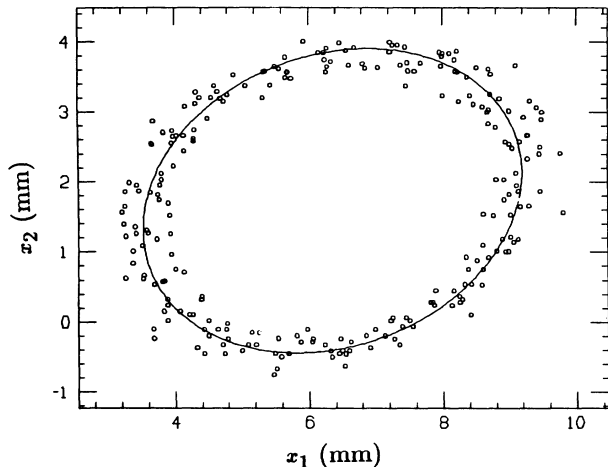


FIG. 2. Plot of horizontal position of the beam centroid measured at BPM2 vs the same measured at BPM1 on a turn-by-turn basis. The curve is a fit to an ellipse.

making this substitution, Eq. (3.4) for p_{x1} becomes

$$p_{x1} = -x_1 \cot \phi_{12} + \frac{\sqrt{\beta_{x1}/\beta_{x2}}}{\sin \phi_{12}} x_2, \quad (3.7)$$

and the equation for a circle in x_1, p_{x1} becomes an equation for an ellipse in the variables x_1 and x_2 , given by

$$\left(-x_1 \cot \phi_{12} + \frac{\sqrt{\beta_{x1}/\beta_{x2}}}{\sin \phi_{12}} x_2 \right)^2 + x_1^2 = 2\beta_{x1}J. \quad (3.8)$$

The values of ϕ_{12} and β_1/β_2 , needed to transform the position variables to the normalized momentum, were determined by fitting experimental data, taken where it is known the motion is linear, to this equation of an ellipse. See Fig. 2 for a typical set of data for which the motion is linear, with the corresponding fit to the ellipse. Alternately, the β functions at each BPM (which are located in quadrupoles) and the phase advance between the BPM's can be measured independently [8].

C. Resonances

The anharmonic terms in Eq. (3.1) of interest are those due to nonlinear perturbations. Nonlinear perturbations in the accelerator include sextupole fields of chromaticity correction sextupoles, the fringe fields of dipoles, and some small higher-order random error multipoles. These anharmonic terms usually do not significantly perturb the particle motion in phase space except when the betatron tunes are near a resonance. For one-dimensional motion the resonance condition is given by $m\nu_x = n$, where m, n are integers.

The Poincaré map deviates from a circle at a resonance condition. Particle motion around stable fixed points (a stable solution to the equation of motion) in phase space bounded by invariant surfaces may occur for nearly integrable Hamiltonian systems. These stable phase-space ellipses around fixed points, called islands, are separated

by the unstable fixed points. The particle phase-space trajectory passing through unstable fixed points is called the separatrix.

1. Third-integer-resonance analysis

The third-integer resonance at $3\nu_x = 11$ was the lowest-order resonance studied. The dynamic aperture was not large enough in the current study to allow one to observe any stable fixed points beyond the one at the origin. Consequently, no island structure is observed in this case. However, the effect of the nonlinearity on motion is easily seen. In Fig. 3 the Poincaré maps for five different kick amplitudes are shown. In this figure it can be seen that the largest kick has placed the beam just beyond the separatrix for stable motion, and the beam intensity falls below our detection threshold in about 70 turns after the kick. For this figure the arithmetic mean of the phase-space points after each kick was taken as the origin. This closely corresponds to the location of the beam before the kick, with a usually small difference resulting from a systematic electronic error in the signal offsets. The deviation of the arithmetic mean of the points after the kick from the measured closed orbit decreases with increasing beam intensity. The largest deviation was seen for the largest kick, where the beam intensity decreased by more than 10 dB. This case is represented by square points in Fig. 3, with the square point near the center being a point before the beam is kicked. The points before the beam is kicked are not used in subsequent analysis.

In order to analyze this motion, a number of assump-

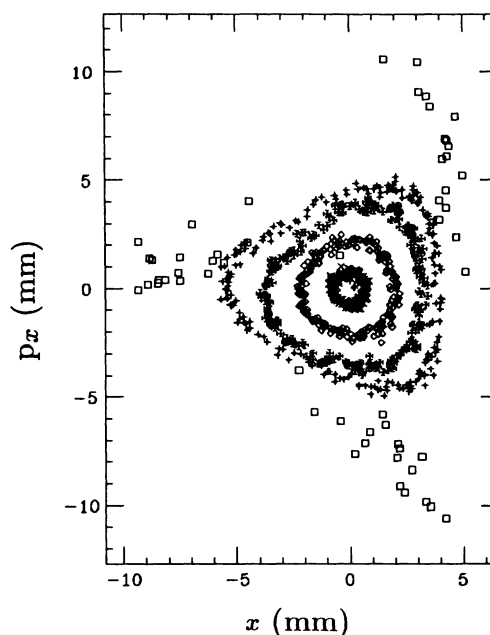


FIG. 3. Poincaré maps for motion near the third-integer resonance for five different kicker amplitudes: 200, 300, 400, 450, and 470 in arbitrary units, increasingly kicker amplitude corresponding to increasingly large J contours.

tions are made. In a storage ring, the magnetic fields are predominately perpendicular to the direction of motion of the charged particles, which means the vector potential \mathbf{A} will have a component in the s direction only. The bending radius ρ of the charged particle is much larger than the x displacement of the particles from the closed orbit, and thus higher-order terms in x/ρ can be omitted. Also, while an electric field is employed to bunch the beam, its effect on transverse motion will be ignored for this discussion. With these assumptions, the Hamiltonian for the system in which the only transverse motion is in the x direction is given by

$$H = -eA_s - \sqrt{p_0^2 - p_x^2}, \quad (3.9)$$

where p_0 is the total momentum, and p_x is the component of the momentum in the x direction. In the median plane of the accelerator, the fields have a relatively simple expansion,

$$A_s = \sum_{n=0} \frac{B^{(n)}}{(n+1)!} x^{n+1}, \quad (3.10)$$

where $n = 0$ is the dipole term, $n = 1$ the quadrupole term, $n = 2$ the sextupole term, etc. The equations of motion resulting from this Hamiltonian, and the linear solutions were already introduced in Sec. III A.

After making the appropriate transformations, it can be shown that the Hamiltonian at the third-order resonance has the form

$$H = J\delta - \frac{(2J)^{3/2}F}{48\pi} \cos[3(\phi + \xi)] + \frac{1}{2}\alpha J^2, \quad (3.11)$$

where $\delta = \nu_{x0} - 3\frac{2}{3}$ and ν_{x0} is the tune in the limit of zero betatron amplitude. The factors F and ξ are related to the strength and location of the sources of the third-order nonlinearities. The factor α is the first-order coefficient of the tune shift caused by the nonlinearity, as a function of J . In studying the third-integer resonance, the term in the Hamiltonian containing α is small and we will neglect it. However, in accelerators where the dynamic aperture is much larger, or in which α is greater, resonance islands could be observed and this term would be necessary to describe the motion.

The Hamiltonian of Eq. (3.11) define contours of constant H in J - ϕ space. The data shown in Fig. 3 are plotted in J - ϕ space in Fig. 4. The solid lines drawn correspond to lines of constant H/F . The values of δ/F and ξ used in these calculations were determined empirically, the value of δ/F was $-0.050\sqrt{\pi}$ mm mrad and the value of ξ was 0° . The corresponding unstable fixed point (UFP), given by $J_{\text{UFP}} = 128\pi^2(\delta^2/F)$ is 3.2π mm mrad.

In Fig. 5 the tune shift for the data pictured in Fig. 3 is shown. From this figure it can be seen that the value of δ is -0.0060 . From this and the empirically determined value of δ/F above, the experimental value of F is about $67 \text{ m}^{-\frac{1}{2}}$.

Assuming that the third-order resonance is driven by sextupole contributions only, the parameters F and ξ in Eq. (3.11) are given by

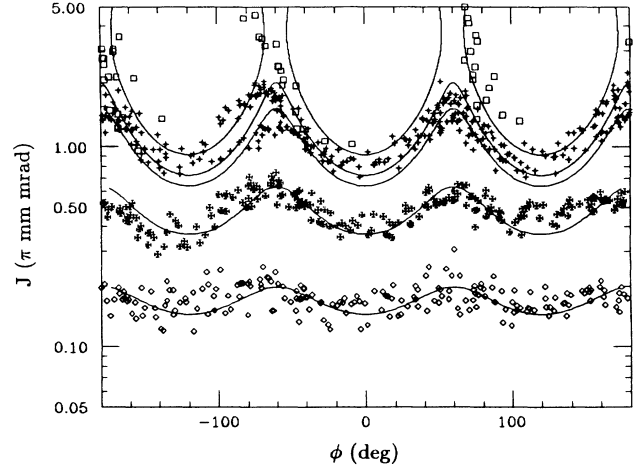


FIG. 4. Data from Fig. 3 shown in J - ϕ space. The contours shown are calculated using Eq. (3.11).

$$F e^{3i\xi} = \oint [\beta(s)]^{3/2} \frac{B''}{B\rho} e^{3i\nu_x\phi(s)} ds. \quad (3.12)$$

The value of F can be found by integrating the sextupole strengths for the different components of the ring. The major contributors of sextupole strength, $S = \frac{B''}{B\rho}$, are the chromaticity correcting sextupoles and the end sextupole fields of the 12 main dipole magnets. The expected contribution to the integral from the sextupole magnets has been evaluated and has a magnitude of about $82 \text{ m}^{-\frac{1}{2}}$. The contribution to the integral due to the sextupole component of field for the bending magnets is more difficult to evaluate. Assuming the sextupole strength at the ends of each dipole magnet, S_d , to be the same, the contribution to the integral due to the dipoles can be evaluated. So, Eq. (3.12) can be written for the current case as

$$F e^{3i\xi} = 82 \text{ m}^{-\frac{1}{2}} e^{-i26^\circ} + S_d (20 \text{ m}^{\frac{5}{2}} e^{+i109^\circ}). \quad (3.13)$$

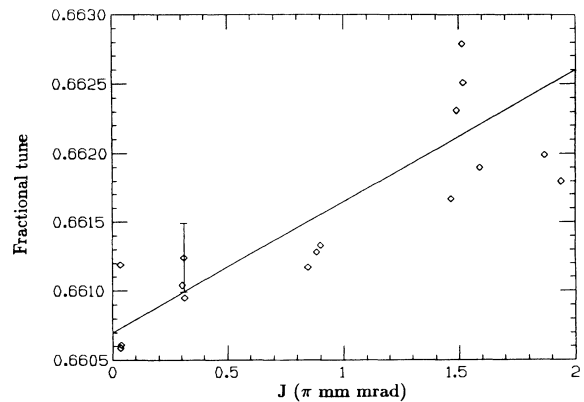


FIG. 5. Plot of the measured tunes for data taken near the third-integer tune, of which the data shown in Fig. 3 are a subset.

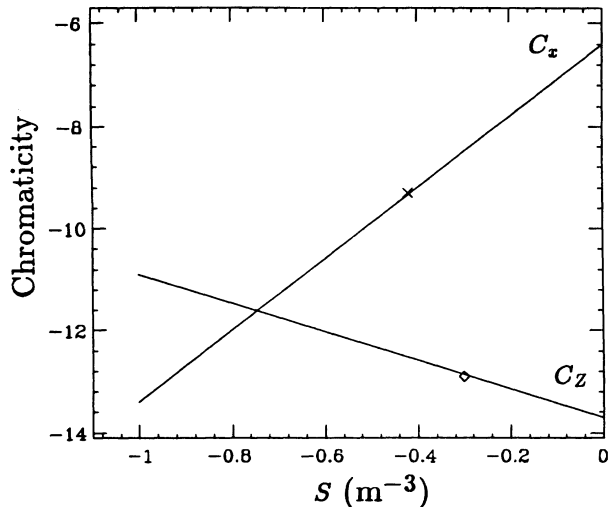


FIG. 6. Graph of the horizontal chromaticity C_x and vertical chromaticity C_z vs the dipole magnet's sextupole strength. The experimentally determined values of C_x and C_z are plotted as points on the two curves.

With a determination of S_d , a comparison of the theoretical values of F and ξ with the measured values can be made. We make an estimate of the required sextupole strength of the bending magnets from the experimentally measured chromaticities.

The sextupole strength of the dipole magnets is deduced from the measured chromaticities C_x and C_z . The chromaticity is the rate at which the tune changes with the change in relative momentum $\Delta p/p$, and it is a function of S for the dipole magnets. In Fig. 6, a graph of chromaticity versus S , computed using the program MAD, is shown. The experimentally measured values of chromaticity are also shown as points on the calculated curves. From this figure, the value of S_d can be deduced to be about -0.4 m^{-3} . Thus the calculated value of F is $88 \text{ m}^{-\frac{1}{2}}$ and ξ is -10° . The discrepancy between these calculated values and the experimental values is a topic of continuing investigation.

2. Linear betatron coupling resonance

In addition to nonlinearities, there are anharmonic terms that have the effect of linearly coupling the horizontal and vertical modes of motion. In the case of linear coupling, the anharmonic term may arise from the skew quadrupole components, or from the solenoidal fields in the cooling region. Then for x and z motion, Eq. (3.1) has the form of two coupled harmonic oscillators,

$$x'' + \omega_x^2 x = -az, \quad z'' + \omega_z^2 z = -ax, \quad (3.14)$$

where a is the coupling constant, ω_x is $2\pi\nu_x f_0$; and similarly ω_z is $2\pi\nu_z f_0$, where f_0 is the revolution frequency. The solutions for the linearly coupled betatron motion can be expressed in terms of the superposition of two eigenmodes,

$$x = Ae^{i\omega_+ t} + Be^{i\omega_- t}, \quad z = Ce^{i\omega_+ t} + De^{i\omega_- t}. \quad (3.15)$$

When the coupling is weak, ω_- and ω_+ are approximately $2\pi f_0 \nu_x$ and $2\pi f_0 \nu_z$. When these two frequencies are relatively near each other, the result is the familiar modulation of the amplitude of the position motion with a frequency equal to the beat frequency, or the difference between the two normal mode frequencies. However, the FFT of the horizontal position for a case with linear coupling would only contain frequencies at ω_+ and ω_- . If the measured signal has some nonlinearity, the frequency spectrum may also contain harmonics of these frequencies and mixtures of frequencies. In Fig. 7, experimental data are shown in a case where the coupling is relatively strong. The modulation in the position oscillation at the beat frequency is evident. The strong linear coupling arises mainly from the solenoidal field of the electron cooling system.

The effect of the coupling on the phase-space plots can be difficult to distinguish from the effect due to a nonlinearity. The data shown in the Poincaré maps of Fig. 8 were taken near three different resonance conditions: In Fig. 8(a) the map is made using data taken with a tune near the seventh-integer resonance, in Fig. 8(b) it is from data taken near the fifth-integer resonance, and for Fig. 8(c) the data was taken near the fourth-integer resonance. For each case shown in this figure, the order of the resonance is evident from the symmetry of the motion in phase space, as well as from the measured tune. While each set of data shown in Fig. 8 has the characteristics of motion due to a nonlinearity, as was described at the beginning of Sec. III C, each can be shown to be primarily due to linear coupling. An example in which both

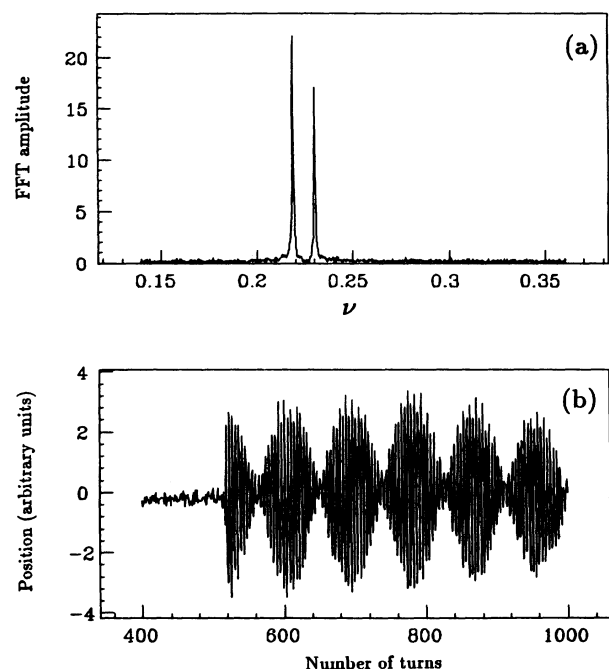


FIG. 7. FFT and x position spectra for a case where coupling is relatively strong.

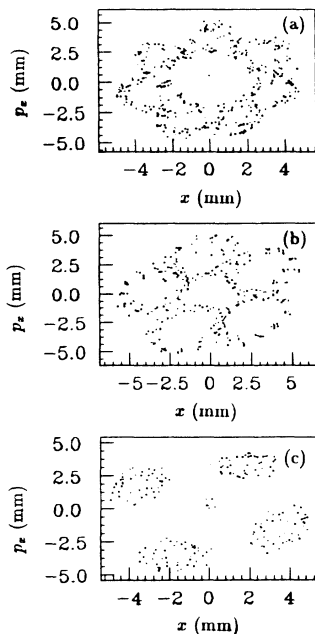


FIG. 8. Poincaré maps for data taken near three different resonance conditions. The data in (a) are taken with a $\nu_x \approx 3\frac{5}{7}$, in (b) $\nu_x \approx 3\frac{4}{5}$, and in (c) $\nu_x \approx 3\frac{3}{4}$.

linear coupling and a nonlinearity contribute strongly to the observed motion will be discussed in Sec. III C 3.

There are several ways of identifying the effect coupling has on motion in one dimension. If an FFT of the x position variable is made, then the two frequencies associated with the x and z tunes are easily determined. In Fig. 9

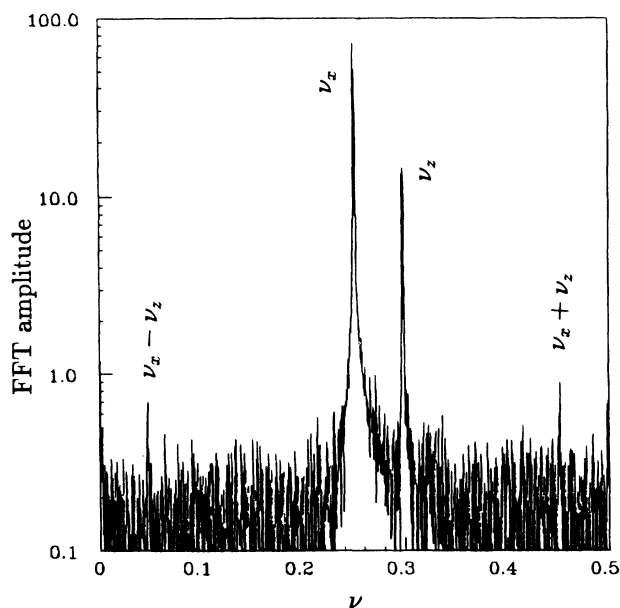


FIG. 9. FFT of the position for the data in Fig. 8(c). The FFT of the position is shown for case where linear coupling dominates. Peaks corresponding to ν_x and ν_z are visible and labeled. Additional labeled peaks are due to a first-order nonlinearity in the position measurement.

the FFT for the x position is shown for the data near the fourth-integer resonance displayed in Fig. 8(c). The ratio of the two strongest peaks in the FFT, corresponding to the x and z tunes, is approximately equal to the square root of the ratio of the integrated phase-space area of the observed islands to the total phase space covered. This is the expected result for motion due to coupling.

While coupling is easy to identify, it complicates the Poincaré map, obscuring the effects of a nonlinear perturbation. Efforts to minimize this effect were made by purposely moving the vertical betatron tune away from the horizontal tune to reduce the magnitude of the betatron coupling. This method was of limited usefulness. For more recent work, a more effective coupling correction scheme utilizing skew quadrupoles has been developed.

3. Fourth-integer-resonance analysis [4]

While coupling produces much more complicated motion in a Poincaré map, the effect of a perturbing nonlinearity can still be observed in favorable cases. Figure 10 shows the Poincaré map for data taken where the betatron tune is $\nu_x = 3.7578$ in the left graph and $\nu_x = 3.7500$ in the right graph. The Poincaré map in the right part of the figure shows that particles were kicked onto the fourth-order resonance islands. A comparison of this Poincaré map to that shown in Fig. 8(c) for a different set of data, also taken near the fourth-integer resonance, reveals that the motion in phase space is more complex in this case. The strength of the perturbing nonlinearity

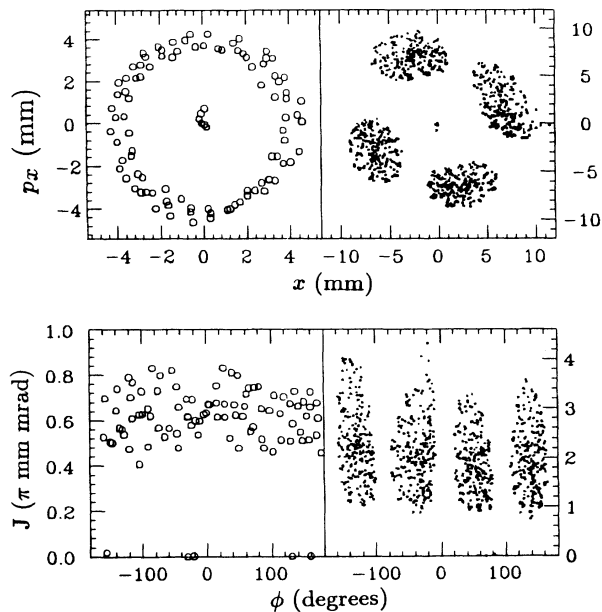


FIG. 10. Poincaré maps in the normal coordinates (x_1, p_{x_1}) at the betatron tunes $\nu_x = 3.7578$ (left) and $\nu_x = 3.7500$ (right) are shown for comparison. The resolution of the measurement is about 0.1 mm. The corresponding maps using the action-angle variables (J_1, ϕ_1) are also shown in the lower part of the figure.

in this case was much stronger. Within an island the particle trajectory, on average, traced out an ellipse around a corresponding stable fixed point. However, this motion is obscured by the motion due to coupling.

The most direct evidence for the presence of the perturbing nonlinearity is found in the FFT spectrum of the betatron motion. The FFT of the x position at the fourth-order resonance, $\nu_x = 3.7500$, is shown in Fig. 11(a). Note that the vertical betatron tune, present due to linear betatron coupling, is also observed at $\nu_z = 5 - 0.3024$. A peak corresponding to the island frequency is present in this spectrum at a very low frequency where it is difficult to measure. The frequency of oscillation around an island's fixed point provides useful information and is somewhat easier to measure by calculating the FFT for a single island, i.e., every fourth turn around the ring for the fourth-integer resonance. Using the same set of data used for the FFT shown in Fig. 11(a), the FFT spectrum of oscillations in a single island is shown in Fig. 11(b). Note that there are two dominant peaks; one located at $\nu_{\text{coupling}} = \nu_x - \nu_z + 1 = 0.0524 \pm 0.0007$ due to linear coupling and another corresponding to the resonance island tune $\nu_{\text{island}} = 0.0013 \pm 0.0007$. The accuracy of the island tune measurement is limited by the available memory in the transient recorders or the lifetime of the beam. The beam completes one oscillation around an island's fixed point after $1/\nu_{\text{island}}$ (about 800 in this case) orbital revolutions, while the oscillation due to coupling occurs in $1/\nu_{\text{coupling}}$ (about 19) orbital revolutions.

As discussed previously, the resonance island ellipse in

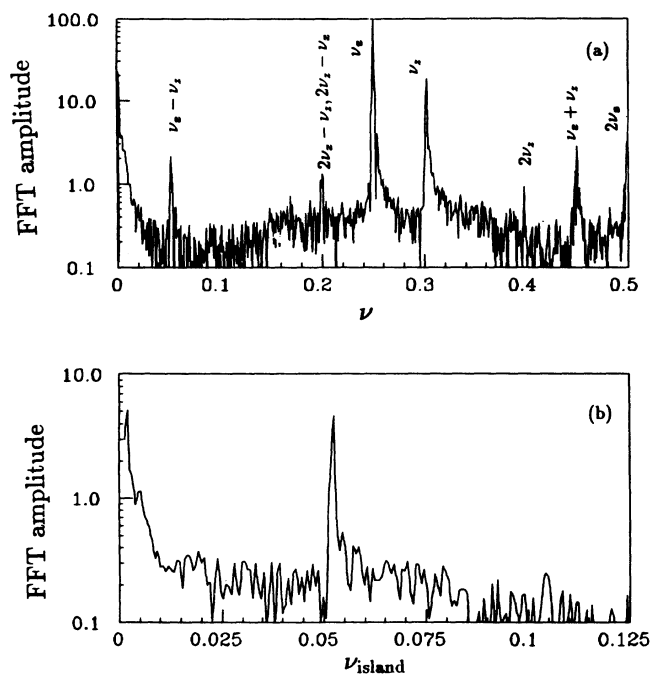


FIG. 11. FFT of the position for the betatron motion at the resonance condition $4\nu_x = 15$ for the data shown in Fig. 10. In (a) the FFT of the position is shown. In (b), the FFT spectrum of every fourth turn, for motion around a fixed point is shown.

the right-hand side of Fig. 10 is obscured by the linear coupling, but now it can be shown that the island structure is retained. The motion is a superposition of the more rapid coupling oscillation and the slower resonance island oscillation. When examined with this perspective, the phase-space trajectory appears as the coupling oscillation winding around a resonance island ellipse (see Fig. 12). For the coupling tune of 0.0524 at the fourth-order betatron resonance condition, it takes five island turns (e.g., the 1st, 5th, 9th, 13th, and 17th orbital turns for the first island, etc.) for the particle to complete one loop around a centroid in the coupling ellipse. A five-island-turn moving average of the phase-space coordinates effectively eliminates the more rapid coupling motion, revealing the slower resonance island oscillation. The moving average traces out an ellipse around the stable fixed point of an island with a characteristic frequency of the island tune, $\nu_{\text{island}} = 0.0013$, which corresponds to a period of over 800 orbital turns or about 200 island turns.

Near an isolated resonance, $m\nu \approx n$, the Hamiltonian can be approximated by [2]

$$H = H_0(J) + g(J) \cos(m\phi - n\theta - \chi). \quad (3.16)$$

Here J and ϕ are the conjugate action-angle variables of the betatron motion, and χ is a phase factor determined by the distribution of nonlinear elements in the accelerator. The betatron tune is given by $\nu(J) = \frac{\partial H}{\partial J} \approx \nu_0 + \alpha J$, where we have used a first-order Taylor series expansion in the action variable with ν_0 as the betatron tune at zero betatron amplitude and α the coefficient of the first-order expansion. The factor $g(J)$ is related to the resonance strength and $\theta = s/R$ is the orbital angle around an accelerator. For the present study, $m = 4$ and $n = 15$.

A canonical transformation with generating function, $F_2(\phi, J_1) = (\phi - \frac{n}{m}\theta)J_1$, can be made to yield a new Hamiltonian,

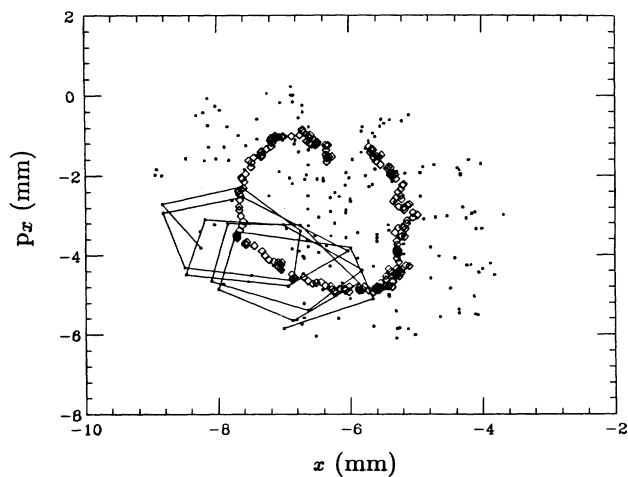


FIG. 12. Phase-space points (dots) of the island in the third quadrant shown on the right-hand side of Fig. 10 are displayed with the corresponding five-island-turn running average (diamonds). The averaged five-island-turn centroids move along an ellipse around a stable fixed point of the fourth-order resonance.

$$\tilde{H} = H_0(J_1) - \frac{n}{m}J_1 + g(J_1) \cos(m\phi_1 - \chi), \quad (3.17)$$

where (J_1, ϕ_1) are the new conjugate action-angle variables with $J_1 = J$ and $\phi_1 = \phi - \frac{n}{m}\theta$. Note here that the new Hamiltonian \tilde{H} is a constant of motion; the particle trajectory follows a contour of constant \tilde{H} . Fixed points of the Hamiltonian are given by $\partial\tilde{H}/\partial J_1 = 0$ and $\partial\tilde{H}/\partial\phi_1 = 0$, i.e., $\nu(J_1) - \frac{n}{m} + g'(J_1) \cos(m\phi_1 - \chi) = 0$ and $\sin(m\phi_1 - \chi) = 0$.

Let J_r be the corresponding action such that the betatron tune satisfies a resonance condition; i.e., $m\nu(J_r) = n$. The Hamiltonian can then be expanded around the resonant action:

$$\tilde{H} = \frac{\alpha}{2}(J_1 - J_r)^2 + g(J_r) \cos(m\phi_1 - \chi) + \dots, \quad (3.18)$$

where constant terms are disregarded, and the first and second partial derivatives of g with respect to J_1 are assumed to be negligible. Thus the equation of motion in the resonance region resembles the equation of motion of a pendulum. The island tune is given by $\nu_{\text{island}} = m\sqrt{|\alpha g|}$ and so the resonance strength is given by $|g| = \nu_{\text{island}}^2 / (m^2|\alpha|)$. The island width, or the maximum difference in the action variables between the stable fixed point and the separatrix, is given by

$$\Delta J = (J_1 - J_r) \approx 2\sqrt{\frac{g(J_r)}{\alpha}} = \frac{2\nu_{\text{island}}}{m\alpha}. \quad (3.19)$$

The ellipses of particle motion around the stable fixed point can be described by the invariant Hamiltonian of Eq. (3.18). Substituting $g = \frac{\nu_{\text{island}}^2}{m^2\alpha}$ in Eq. (3.18), the parameter α can be obtained through matching the particle trajectory with the contour of the Hamiltonian. In Fig. 13 a (J, ϕ) plot of the data, after taking a five-island-turn moving average in each island to re-

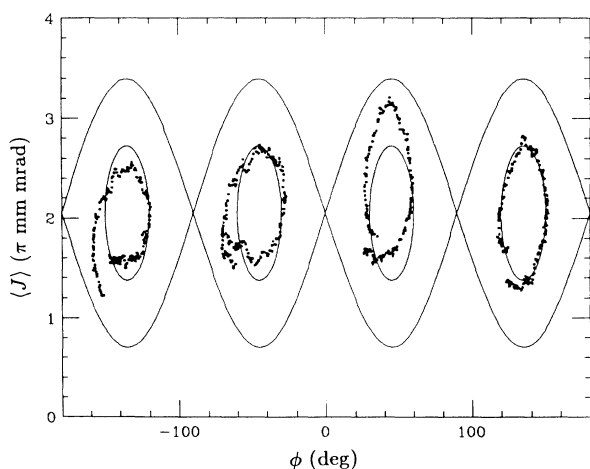


FIG. 13. Stable ellipse around island fixed points in the action angle variable is fit with the Hamiltonian of Eq. (3.18) with $\nu_{\text{island}} = 0.0013$. The action and angle variables are obtained from averaging every five island turns in each island in order to eliminate the effect of the coupling resonance. We found $\alpha = 0.0005 \pm 0.0001$ (π mm mrad) $^{-1}$. The calculated ellipse in the present figure used $\alpha = 0.00048$ (π mm mrad) $^{-1}$.

move the coupling motion, clearly shows the island ellipses. Using the Hamiltonian in Eq. (3.18), we find $\alpha = 0.0005 \pm 0.0001$ (π mm mrad) $^{-1}$. The corresponding separatrix is also shown in Fig. 13. The resonance strength g is $2.0 \times 10^{-4} \pi$ mm mrad in this instance.

The value of g obtained experimentally can be compared with the value of g calculated using the program HARMON [9]. As for the calculation done in the third-order analysis, using the known sextupole strengths for the chromatic sextupoles and assuming the sextupole strength in the dipole magnets to be -0.4 m $^{-3}$ as deduced from the chromaticity, the resonance strength g can be found from the equation,

$$g = 4R\nu_{4,0,0,0,15}\langle J_x^2 \rangle, \quad (3.20)$$

where R is the radius of the ring, and $\nu_{4,0,0,0,15}$ is the parameter calculated by HARMON. The value of g obtained from this calculation is about $3.1 \times 10^{-4} \pi$ mm mrad, which is larger than the value of g obtained from the fit to the data. The value calculated for α is about 4×10^{-5} , or about one order of magnitude smaller than the value obtained from the fit. This discrepancy can be resolved if there is sufficient octupole strength in the cooler quadrupoles. The origin of these octupole fields may arise from the coil configuration at the end of these magnets.

For comparison, the parameter α can also be obtained from the slope of the betatron tune as a function of the average action for the motion, $\langle J \rangle$. The different values of $\langle J \rangle$ resulted from kicking the beam with different kicker strengths. In Fig. 14, measured tunes obtained from a range of kick amplitudes are plotted against $\langle J \rangle$, where the data shown in Fig. 13 determine one point in this graph. While the errors for the individual points are relatively large due to the limitation that a short beam lifetime placed on obtaining enough data to perform an accurate FFT, the result of a least-squares fit to a line gives a value for α of 6.5×10^{-4} (π mm mrad) $^{-1}$.

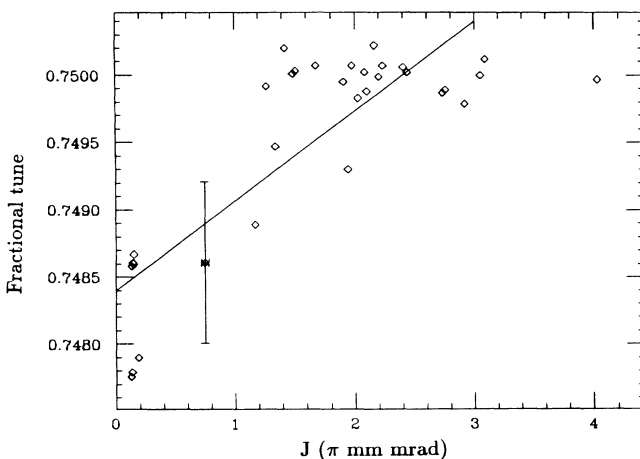


FIG. 14. Plot of ν_x vs the average value of J produced by a variety of kick amplitudes with a representative error bar. The slope of a least-squares fit line is 0.00065, which corresponds to the parameter α .

4. Synchrotron oscillations near fourth-order resonance

The chromatic sextupoles were excited to produce the fourth-order resonance islands discussed in the last section. These sextupoles can also be adjusted to minimize the fourth-order resonance strength. While this condition was not interesting in terms of nonlinear motion, it did exhibit another interesting feature. In Fig. 15 the time evolution of the motion in phase space near the fourth-order resonance condition is shown when the resonance strength is small. These data imply that there is a time-dependent shift in the betatron tune near resonance. By tracking the location for a single "island" by using a moving average to remove the coupling motion, as was done above, the phase for every fourth turn is seen to have the form

$$\phi = 2\pi(\nu_x - 3\frac{3}{4})n + A \sin(2\pi\nu_{\text{syn}}n + \chi), \quad (3.21)$$

where ν_{syn} is the measured synchrotron frequency, n is the turn number, and χ , ν_x , and A are to be determined from a fit to the data. An example of this is shown in the plot of the average phase of the island, $\langle\phi\rangle$, versus turn number in Fig. 16. Thus the measured betatron phase is composed of two terms; one term is related to the deviation of the betatron tune from the fourth-order resonance condition, and the second term is due to the coherent synchrotron motion of the bunch. The second term may be understood in terms of the chromaticity of the

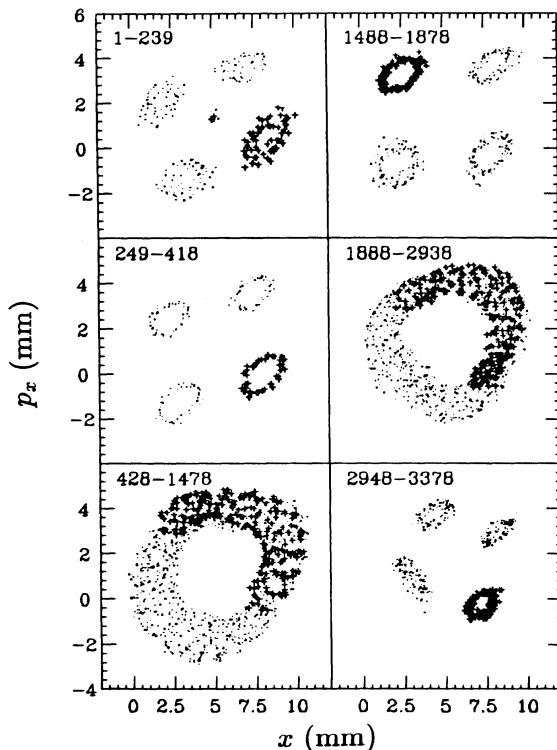


FIG. 15. Time series of Poincaré maps for data taken near the fourth-integer resonance. Note the motion of the "island" appears periodic. The islands in this case arise due to linear betatron coupling.

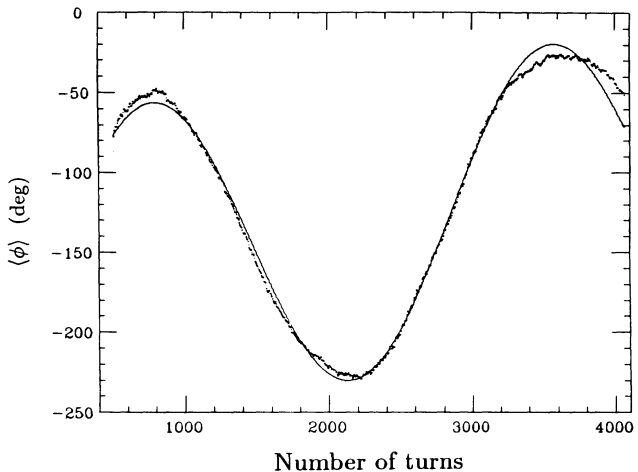


FIG. 16. Plot of the average phase for a single fourth-integer island pictured in Fig. 15 vs the turn number.

machine and the small-amplitude oscillations in longitudinal phase space, or coherent synchrotron oscillations, resulting from the particle bunching in the rf cavity. The chromaticity of the storage ring converts the oscillations in momentum to oscillations in betatron tune, resulting in the oscillations in phase observed.

By measuring the slope of line about which this synchrotron oscillation occurs in the graph of island phase versus accelerator turns, the betatron tune was determined more precisely than was possible with the FFT of the position from one BPM alone. Provided that linear betatron motion is assumed for this analysis, the slope of this line divided by 2π represents the deviation of the tune from exactly 3.75. Although a more direct method exists for determining the magnitude of the coherent relative momentum oscillation, these data can also be used for this purpose. If the chromaticity is well known, a relatively accurate measure of the collective relative momentum oscillation is given by $\Delta p/p = A\nu_{\text{syn}}/C_x$. For the case shown in Fig. 16 the tune is 3.75004, and the amplitude of the coherent momentum oscillation is about 6×10^{-5} for a chromaticity of $C_x \approx -10$.

While coherent synchrotron motion seems to quite reasonably explain the motion observed, it should be noted that the possibility that some other effect, such as tune modulation by oscillations in quadrupole power supplies, cannot yet be ruled out. This awaits confirmation in future experiments where more direct measurements of the coherent momentum oscillations are made in addition to the transverse phase-space measurements.

IV. CONCLUSION

In conclusion, we have studied particle motion in an accelerator near the third-, fourth-, fifth-, and seventh-integer resonances. We have identified and measured the properties of third-order nonlinear motion, and of fourth-order nonlinear resonance islands. In addition, the

motion in phase space attributable to betatron coupling and to coherent oscillations in momentum was identified. This motion was used to produce a more accurate measure of the tune than the FFT alone, and, assuming no other sources of tune modulation, to measure the coherent oscillation in $\Delta p/p$.

An interesting feature of the resonance islands observed was that betatron coupling does not destroy the structure of one-dimensional resonance islands. Experimental data were used to determine fourth-integer-resonance island parameters ν_{island} , J_r , and α . The Hamiltonian for the particle motion near the fourth-integer-resonance region was experimentally determined.

In experimental work done very recently at IUCF, the reduction of linear coupling of transverse modes of motion has produced even greater detail, and shows promise of revealing higher-order terms in J for the Hamiltonian. In addition, current efforts include expanding these measurements from one to two dimensions. Experimentally derived Hamiltonians, including more and more higher-order terms, may allow more reliable predictions of particle motion. These experimental nonlinear-beam-dynamics studies may prove to be useful in an effort to understand the dynamic aperture and the long-term behavior of particle motion for future colliders, such as the SSC and RHIC.

* Present address: Stanford Linear Accelerator Center, Bin 26, P.O. Box 4349, Stanford, CA 94309.

- [1] A.M. Sessler, in *Nonlinear Dynamics and Particle Acceleration (Tsukuba, Japan, 1990)*, AIP Conf. Proc. No. 230 (AIP, New York, 1991), p. 165.
- [2] R. Ruth, in *Physics of Particle Accelerators (Fermi National Accelerator Laboratory, 1984)*, edited by Melvin Month and Margaret Deines, AIP Conf. Proc. No. 153 (AIP, New York, 1984), p. 150; R.L. Warnock, R.D. Ruth, and K. Ecklund, in *Proceedings of the IEEE Particle Accelerator Conference, Chicago, 1989*, edited by Floyd Bennett and Joyce Kopta (IEEE, New York, 1989), p. 1325; A.J. Dragt, in *Physics of High Energy Particle Accelerators*, Published Lectures from the Summer School on High Energy Particle Accelerators, edited by R.A. Carrigan, F.R. Huson, and M. Month, AIP Conf. Proc. No. 87 (AIP, New York, 1982), p. 147; L. Michelotti, in *Physics of Particle Accelerators (Fermi National Accelerator Laboratory, 1984)*, Proceedings of the Fifth Annual U.S. Particle Accelerator School, edited by Melvin Month and Margaret Deines, AIP Conf. Proc. No. 153 (AIP, New York, 1987), p. 236; G. Guignard, CERN Report No. 78-11 (1978).
- [3] A. Chao *et al.*, Phys. Rev. Lett. **61**, 2752 (1988); M. Cornacchia and L. Evans, Part. Accel. **19**, 125 (1986); L. Evans *et al.*, in *Proceedings of the European Particle Accelerator Conference, Rome, 1988*, edited by S. Tazzari (World Scientific, Teaneck, NJ, 1989), p. 618; J. Gareyte, A. Hilaire, and F. Schmidt, in *Proceedings of the IEEE Particle Accelerator Conference, Chicago, 1989* (Ref. [2]), p. 1376; L. Evans *et al.*, *ibid.*, p. 1403; L. Evans, CERN Report No. SPS/83-38 (unpublished); P.L. Morton *et al.*, IEEE Tran. Nucl. Sci. **NS-32**, 2291 (1985); D.A. Edwards, R.P. Johnson, and F. Willeke, Part. Accel. **19**, 145 (1986).
- [4] S.Y. Lee *et al.*, Phys. Rev. Lett. **67**, 3768 (1991).
- [5] E.D. Courant and H.S. Snyder, Ann. Phys. **3**, 1 (1958).
- [6] T.J. Ellison, C.M. Fox, and S.W. Koch, Nucl. Instrum. Methods **B24/25**, 873 (1987).
- [7] M.S. Ball, T.J. Ellison, and B.J. Hamilton, in *Conference Record of the 1991 IEEE Particle Accelerator Conference, San Francisco*, edited by Loretta Lizama and Joe Chew (IEEE, New York, 1991), p. 1210.
- [8] R. Littauer, in *Physics of High Energy Particle Accelerators (Stanford Linear Accelerator Center, Stanford University, California)*, AIP Conf. Proc. No. 105 (AIP, New York, 1983), p. 869.
- [9] M. Donald and D. Schofield, CERN LEP Note 420 (unpublished).

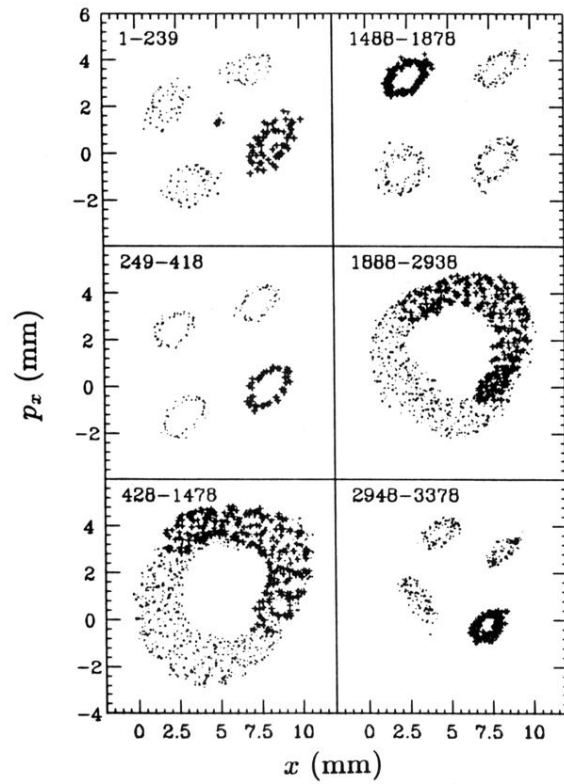


FIG. 15. Time series of Poincaré maps for data taken near the fourth-integer resonance. Note the motion of the “island” appears periodic. The islands in this case arise due to linear betatron coupling.

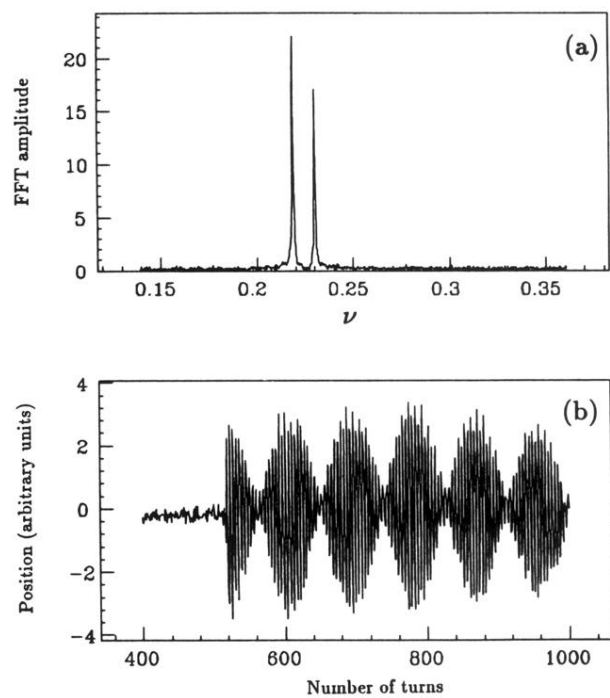


FIG. 7. FFT and x position spectra for a case where coupling is relatively strong.